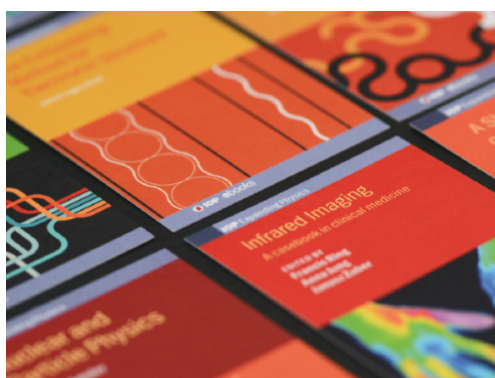Astro Ltd.

LETTER • OPEN ACCESS

3D Mueller-matrix-based azimuthal invariant tomography of polycrystalline structure within benign and malignant soft-tissue tumours

To cite this article: Motahareh Peyvasteh *et al* 2020 *Laser Phys. Lett.* **17** 115606

View the article online for updates and enhancements.

IOP ebooks™

Bringing together innovative digital publishing with leading authors from the global scientific community.

Start exploring the collection−download the first chapter of every title for free.

Letter

3D Mueller-matrix-based azimuthal invariant tomography of polycrystalline structure within benign and malignant soft-tissue tumours

Motahareh Peyvasteh[1]**, Liliya Tryfonyuk**[2]**, Vladimir Ushenko**[3]**, Anastasia-Vira Syvokorovskaya**[2]**, Alexander Dubolazov**[3]**, Oleg Vanchulyak**[2]**, Alexander Ushenko**[3]**, Yuri Ushenko**[3]**, Mykhailo Gorsky**[3]**, Maxim Sidor**[3]**, Yuriy Tomka**[3]**, Iryna Soltys**[3]**, Alexander Bykov**[1] **and Igor Meglinski**[1,4,5,6,7,*]

[1] Optoelectronics and Measurement Techniques Laboratory, University of Oulu, Oulu, Finland
[2] Department of Forensic Medicine, Bukovinian State Medical University, Chernivtsi, Ukraine
[3] Optics and Publishing Department, Chernivtsi National University, Chernivtsi, Ukraine
[4] Interdisciplinary Laboratory of Biophotonics, National Research Tomsk State University, Tomsk, Russia
[5] Institute of Engineering Physics for Biomedicine (PhysBio), National Research Nuclear University 'MEPhI', Moscow, Russia
[6] Department of Histology, Cytology and Embryology, Institute of Clinical Medicine N V Sklifosovsky, I M Sechenov First Moscow State Medical University, Moscow, Russia
[7] College of Engineering and Physical Sciences, Aston University, Birmingham, United Kingdom

E-mail: i.meglinski@aston.ac.uk

CrossMark

Abstract

We introduce a method of azimuthally invariant 3D Mueller-matrix (MM) layer-by-layer mapping of the phase and amplitude parameters of anisotropy of the partially depolarizing layers of benign (adenoma) and malignant (carcinoma) prostate tumours. The technique is based on the analysis of spatial variations of Mueller matrix invariant (MMI) of histological sections of benign (adenoma) and malignant (carcinoma) tissue samples. The phase dependence of magnitudes of the first-to-fourth order statistical moments is applied to characterize 3D spatial distributions of MMI of linear and circular birefringence and dichroism of prostate tumours. The high order statistical moments and phase sections of the optimal differentiation of the polycrystalline structure of tissue samples are revealed. The obtained results are compared with the results obtained by conventional methods utilizing polarized light, including 2D and 3D Mueller matrix imaging.

---

* Author to whom any correspondence should be addressed

1. Introduction

Presently, the methods and means of polarisation-based diagnostics of biological tissues are extensively used in biomedical optics [1–4], including a number of subjects, such as: investigation of scattering matrices [5–9], polarization modeling of Monte Carlo [10–13], polarization spectroscopy [14–16], Mueller-matrix (MM) polarimetry [17–21], polar decomposition of MMs [22, 23], 2D MM mapping [24–27] within the framework of various model approximations [28–31] and other.

The variety of these polarization methods combines following common points:

- The use of the MM formalism [4, 6, 9, 15, 17, 32, 33].
- The resulting MMs are represented either in 1D ('indicatrices' [2, 5, 8, 9, 14, 19]) or in 2D ('MM images' [3, 18, 20, 21, 34, 35]) formats.
- The azimuthal dependence upon rotation of the sample around the axis of the 12th probe of the 16 elements of the MM [17–21, 24, 36, 37].
- Studies of MMs is carried out within the framework of two boundary approximations—optically thin (nondepolarizing [19–21]) layers and diffuse (depolarizing [3, 19, 26, 27, 34, 35]) objects.
- Almost complete lack of information about 3D distributions of matrix elements [32, 33].

Therefore, it is actually to develop 3D azimuthally invariant MM polarimetry of the most common type of objects—partially depolarizing biological tissues. The basis for this can be the joint use of probing and reference coherent beams. This will ensure the possibility of obtaining layered MM images based on the synthesis of methods:

- 2D mapping of Mueller-matrix invariants (MMIs) of biological layers—azimuthally independent distributions of matrix elements or their analytical combinations [24, 36, 37];
- digital holographic restoration of distributions of complex amplitudes of the object field of such layers [32, 33].

Our article is aimed at the development and experimental validation of the diagnostic effectiveness of the method of azimuthally invariant MM tomography of the polycrystalline structure of histological sections of biopsy of benign and malignant tumors of the prostate.

2. Brief theory of the method

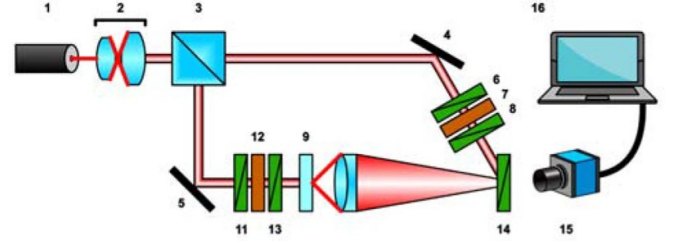In [24, 35–39], it was shown that the following matrix elements and their combinations are azimuthally invariant.

Figure 1. Optical scheme of polarization interferometry of 3D distributions of MM elements. Explanations are in the text.

$$\{F\} == \left\| \begin{matrix} \mathbf{F}_{11} & F_{12} & F_{13} & F_{14} \\ F_{21} & F_{22} & F_{23} & F_{24} \\ F_{31} & F_{32} & F_{33} & F_{34} \\ \mathbf{F}_{41} & F_{42} & F_{43} & \mathbf{F}_{44} \end{matrix} \right\| \Rightarrow \begin{cases} \mathbf{F}_{11}(\Theta) = \mathbf{const}; \\ \mathbf{F}_{14}(\Theta) = \mathbf{const}; \\ \mathbf{F}_{41}(\Theta) = \mathbf{const}; \\ \mathbf{F}_{44}(\Theta) = \mathbf{const}; \end{cases}$$

$$\Downarrow$$

$$\begin{cases} [\mathbf{F}_{22} + \mathbf{F}_{33}](\Theta) \equiv \mathbf{MMI}_{22;33}(\Theta) = \mathbf{const}; \\ [\mathbf{F}_{23} - \mathbf{F}_{32}](\Theta) \equiv \mathbf{MMI}_{23;32}(\Theta) = \mathbf{const} \end{cases} \tag{1}$$

where Θ is the angle of rotation of the sample.

In [40–46], the interrelations between the MMI (relation (1)) and averaged over the thickness (**l**) of the biological layer by 2D parameters of linear (**LB**) and circular (**CB**) birefringence.

$$\begin{cases} \mathbf{F}_{44} \equiv \mathbf{MMI}_{44} \sim \cos \mathbf{LB}; \\ \Delta \mathbf{M} = \dfrac{\mathbf{MMI}_{23;32}}{\mathbf{MMI}_{22;33}} \sim tg\mathbf{CB} \end{cases} \tag{2}$$

and dichroism (**LD**, **CD**)

$$\mathbf{F}_{41} = (1 - \mathbf{LD}) \sin \mathbf{LB} \tag{3}$$

$$\mathbf{F}_{14} = 4\sqrt{\mathbf{LD}} \cos \mathbf{LB} \frac{\mathbf{CB}}{1 + \mathbf{CB}^2} \tag{4}$$

Figure 1 presents the optical arrangement for 3D MM polarimetry of biological layers. Parallel ($\varnothing = 2 \times 10^3 \ \mu$m) beam of He–Ne ($\lambda = 0.6328 \ \mu$m) laser 1, formed by optical collimator 2 by means of 50/50 beamsplitter 3, divided on illuminating and reference ones.

Illuminating laser beam is directed through the polarization filter 5–7 on the sample of biological layer 8. Polarization-inhomogeneous image of the sample 8 by means of strain-free objective 9 (Nikon CFI Achromat P, focal distance—30 mm, numerical aperture—0,1, magnification—4x) is projected in the plane of digital camera 14 (The Imaging Source DMK 41AU02.AS, monochrome 1/2″ CCD, Sony ICX205AL (progressive scan); resolution—1280 × 960; sizes

of light-sensitive plate—7600 × 6200 μm; sensitivity—0,05 lx; dynamic range—8 bit, SNR—9 bit). Reference laser beam by means of reflected mirror 4 is directed through the polarization filter 10–12 in the plane of polarization-inhomogeneous image of sample 8. As the result the interference pattern registered by digital camera 14 is formed. Formation of different polarization states of illuminating and reference beams is created by both polarization filters 5–7 and 10–12, each of them consists of two linear polarizers (B + W Kaesemann XS-Pro Polarizer MRC Nano) and quarterwave plate (Achromatic True Zero-Order Waveplate).

The technique of polarization-interference measurements of MM elements consists in the following sequence of operations:

- Formation of six polarization states $((0^0 - 0^0);(90^0 - 90^0); (45^0 - 45^0);(135^0 - 135^0);(\otimes - \otimes);(\oplus - \oplus))$ in both illuminating and reference laser beams. Here $\otimes, \oplus$ denote right and left circulations correspondingly.
- Registration of each partial interference pattern after passing through polarizer-analyzer 13 with following sequence of orientations of it transmission plane $\Omega = 0^0; \quad \Omega = 90^0$.

Thus, by experimental measurement of the set of coordinate distributions $\left(\mathbf{q} \equiv \begin{cases} \mathbf{F}_{14;41;44}\left(\mathbf{x} \times \mathbf{y} \right); \\ \Delta\mathbf{M}\left(\mathbf{x} \times \mathbf{y} \right) \end{cases} \right)$, it is possible to obtain azimuthally invariant information about the polarization manifestations of the phase and amplitude anisotropy of biological tissues.

The basis for the determination of a series of layered distributions of $\mathbf{q}\left(\mathbf{x}, \mathbf{y}, \mathbf{z} \right)$ is the use of a reference laser radiation wave, which is superimposed on the polarization-inhomogeneous image of the biological layer [31, 32].

The resulting interference pattern is recorded with a digital camera.

Further, apply Fourier transform to interference pattern and using the inverse Fourier transform obtained the distributions of complex amplitudes $|\mathbf{A_x}|$; $|\mathbf{A_y}| \exp i\left(\delta_y - \delta_x \right)$ in different phase planes ($\phi_j = \left(\delta_y - \delta_x \right)_j = \frac{2\pi}{\lambda} z; \quad 0 \leqslant z \leqslant l$) of the object field with an arbitrary step $\Delta\phi_{j=0.p}$.

In each phase plane $\phi_j(x,y)$, for a series of planar (with azimuths $0^0, 90^0, 45^0$) and the right of circularly ($\otimes$) polarized irradiating beams, the distributions of Stokes vector $VS_i^{\left(0^0, 90^0, 45^0, \otimes \right)}$ and MMI are calculated.

$$\begin{cases} VS_1^{\left(0^0, 90^0, 45^0, \otimes \right)} = \left(|\mathbf{A_x}|^2 + |\mathbf{A_y}|^2 \right)^{\left(0^0, 90^0, 45^0, \otimes \right)}; \\ VS_2^{\left(0^0, 90^0, 45^0, \otimes \right)} = \left(|\mathbf{A_x}|^2 - |\mathbf{A_y}|^2 \right)^{\left(0^0, 90^0, 45^0, \otimes \right)}; \\ VS_3^{\left(0^0, 90^0, 45^0, \otimes \right)} = 2\,\mathrm{Re}\,|\mathbf{A_x}\mathbf{A_y^*}|^{\left(0^0, 90^0, 45^0, \otimes \right)}; \\ VS_4^{\left(0^0, 90^0, 45^0, \otimes \right)} = 2\,\mathrm{Im}\,|\mathbf{A_x}\mathbf{A_y^*}|^{\left(0^0, 90^0, 45^0, \otimes \right)} \end{cases} \left(\phi_j \right) \tag{5}$$

$$\begin{aligned} \mathbf{F}_{44}\left(\phi_j \right) &= \left(VS_4^{\otimes} - VS_4^{\oplus} \right)\left(\phi_j \right) \\ &= 2\left(\mathrm{Im}\,|\mathbf{A_x}\mathbf{A_y^*}|^{(\otimes)} - \mathrm{Im}\,|\mathbf{A_x}\mathbf{A_y^*}|^{(\oplus)} \right)\left(\phi_j \right) \end{aligned} \tag{6}$$

$$\begin{aligned} \mathbf{\Delta M}\left(\phi_j \right) &= \frac{\left(VS_2^{45} - VS_2^{135} \right) - \left(VS_3^0 - VS_3^{90} \right)}{\left(VS_2^0 - VS_2^{90} \right) + \left(VS_3^{45} - VS_3^{135} \right)}\left(\phi_j \right) = \\ &= \left[\frac{\left(\left(|\mathbf{A_x}|^2 - |\mathbf{A_y}|^2 \right)^{(45)} - \left(|\mathbf{A_x}|^2 - |\mathbf{A_y}|^2 \right)^{(135)} \right) - 2\left(\mathrm{Re}\,|\mathbf{A_x}\mathbf{A_y^*}|^{(0)} - \mathrm{Re}\,|\mathbf{A_x}\mathbf{A_y^*}|^{(90)} \right)}{\left(\left(|\mathbf{A_x}|^2 - |\mathbf{A_y}|^2 \right)^{(0)} - \left(|\mathbf{A_x}|^2 - |\mathbf{A_y}|^2 \right)^{(90)} \right) + 2\left(\mathrm{Re}\,|\mathbf{A_x}\mathbf{A_y^*}|^{(45)} - \mathrm{Re}\,|\mathbf{A_x}\mathbf{A_y^*}|^{(135)} \right)} \right]\left(\phi_j \right) \end{aligned} \tag{7}$$

$$\begin{aligned} \mathbf{F}_{14}\left(\phi_j \right) &= \left(VS_1^{\otimes} - VS_1^{\oplus} \right)\left(\phi_j \right) \\ &= \left(\left(|\mathbf{A_x}|^2 + |\mathbf{A_y}|^2 \right)^{(\otimes)} - \left(|\mathbf{A_x}|^2 + |\mathbf{A_y}|^2 \right)^{(\oplus)} \right)\left(\phi_j \right) \end{aligned} \tag{8}$$

$$\begin{aligned} \mathbf{F}_{41}\left(\phi_j \right) &= \left(VS_4^0 + VS_4^{90} \right)\left(\phi_j \right) \\ &= 2\left(\mathrm{Im}\,|\mathbf{A_x}\mathbf{A_y^*}|^{(0)} + \mathrm{Im}\,|\mathbf{A_x}\mathbf{A_y^*}|^{(90)} \right)\left(\phi_j \right) \end{aligned} \tag{9}$$

The optical scheme and the technique of experimental measurements of the MMI aggregate of biological layers (relations (6)–(9)) are described in detail and presented in [19–21, 24, 36, 37].

3. Principles of 3D azimuthally-invariant MM differential diagnostics

To determine the diagnostic effectiveness of azimuthally-invariant 3D MM tomography, two representative groups of patients were formed with 28 samples of tumors in each. For each operably extracted tumor 16 histological sections were prepared with the geometric dimensions which are commensurable with the diameter of illuminating laser beam (∼2000 × 2000 μm): (i) benign tumor (adenoma—16 samples)—group 1 (attenuation coefficient $0,79 \prec \tau \prec 0,85$, degree of depolarization $43\% \prec \Lambda \prec 48\%$); (ii) malignant
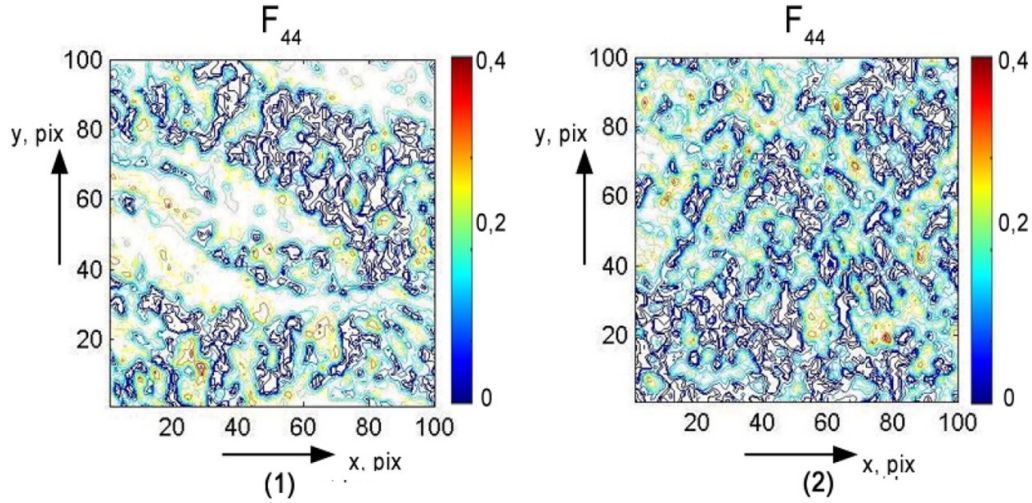
Figure 2. Coordinate distributions of MMI $\mathbf{F_{44}}$, characterizing the linear birefringence **LB** of adenoma samples (fragment (1)) and carcinomas (fragment (2)) of the prostate.

tumor (carcinoma—16 samples)—group 2 $(0,81 \prec \tau \prec 0,84, 45\% \prec \Lambda \prec 47\%)$.

The optical technology of differential diagnostics of such samples includes the following steps:

(a) Definition of a series of 'phase' layered images $(m \times n$—number of pixels of a digital camera) of 3D MMI distributions $\{\mathbf{F_{44}}; \mathbf{\Delta M}; \mathbf{F_{41}}; \mathbf{F_{14}}\}$ $(\phi_1 = 0,3\,rad; 2\phi_1, 6\phi_1)$ within both groups of samples.

(b) The statistical moments of the first-fourth order $\mathbf{Z_{i=1;2;3;4}} \{[\mathbf{F_{44}}; \mathbf{\Delta M}; \mathbf{F_{41}}; \mathbf{F_{14}}] (\phi_k, m \times n)\}$ are calculated for each distribution of MMI in each 'phase' section ϕ_j.

(c) The 'phase' planes (ϕ^*), in which the maximum differences between the values of the statistical moments $(\mathbf{\Delta Z_{i=1;2;3;4}^*} \equiv \mathbf{\Delta Z_{i=1;2;3;4}}(\phi^*) \rightarrow \max)$ are realized, are determined.

(d) In the 'phase' plane ϕ^*, the mean $\mathbf{\Delta \bar{Z}_{i=1;2;3;4}^*}$ and error $\boldsymbol{\sigma}(\mathbf{\Delta Z_i^*})$ of the ensemble of values $(\mathbf{Z_{i=1;2;3;4}})_{k=1,2,r}$ that characterize the distributions $[\mathbf{F_{44}}; \mathbf{\Delta M}; \mathbf{F_{41}}; \mathbf{F_{14}}] (\phi_k, m \times n)$ within the set (r) of the histological sections of biopsy of prostate tumors from group 1 and group 2 are determined.

(e) For the purpose of possible clinical application for each of the statistical moments $\mathbf{Z_{i=1;2;3;4}}$ sensitivity (**W**); specificity (**P**) and balanced accuracy (**T**) of the 3D azimuthally-invariant MM tomography are determined [47].

$$\begin{cases} \mathbf{W} = \dfrac{k_1}{k_1 + k_2} 100\%; \\[2ex] \mathbf{P} = \dfrac{g_1}{g_1 + g_2} 100\%; \\[2ex] \mathbf{T} = \dfrac{\mathbf{W} + \mathbf{P}}{2} 100\%, \end{cases} \qquad (10)$$

where k_1 and k_2 is the number of correct and incorrect diagnoses within group 2; g_1 and g_2- the same within group.

4. Analysis and discussion of the experimental results

In figures 2–4 shows maps of the phase cross sections (ϕ_j) of the MMI distributions $(m \times n = 100\,pix \times 100\,pix; 1\,pix = 10\,\mu m)$　　　$\mathbf{F_{44}}$ $(\phi^* = 0.45\,rad, m \times n)$ (figure 1); $\mathbf{\Delta M}$ $(\phi^* = 0.45\,rad, m \times n)$ (figure 2); $\mathbf{F_{41}}$ $(\phi^* = 0.75\,rad, m \times n)$ (figure 3) and $\mathbf{F_{14}}$ $(\phi^* = 0.75\,rad, m \times n)$ (figure 4). The MMI $[\mathbf{F_{44}}; \mathbf{\Delta M}]$ $(m \times n)$ maps are obtained for the $\phi^* = 0.45\,rad$ phase section. Coordinate distributions of MMI $[\mathbf{F_{41}}; \mathbf{F_{14}}]$ $(m \times n)$ are obtained for $\phi^* = 0.75\,rad$.

Let us analyze the results obtained from the physical point of view.

For the distributions of linear **LB** (figure 1) and circular **CB** (figure 2) birefringence of samples of both types due to different pathology of the prostate tissue, the following transformations of the polycrystalline structure take place.

A benign tumor contains a developed newly formed linear birefringent network, which is formed due to an increase in the concentration of optically active protein molecules [2–4, 19–21, 34, 35].

Oncological processes are accompanied by destruction of the fibrillar network. Optically, this is manifested in a decrease in the structural anisotropy—linear birefringence (**LB**↓) of the prostate tissue. Due to this, the mean and range of variation of the random variables of the MMI distribution $\mathbf{F_{44}}(\phi, m \times n) \sim \cos \mathbf{LB}$ (relation (2)) increases (figure 2, fragments (1), (2)). In parallel with this, the concentration of optically active protein molecules decreases due to necrosis. As a result, for the distribution $\mathbf{\Delta M}(\phi, m \times n) \sim \tan \mathbf{CB}$ (relation (2)), there is a reverse scenario—a decrease in the mean and range of variation of the random variables of this MMI (figure 2, fragments (1), (2)).

Within the framework of the statistical analysis of MMI distributions of the phase anisotropy of prostate tumors, one can
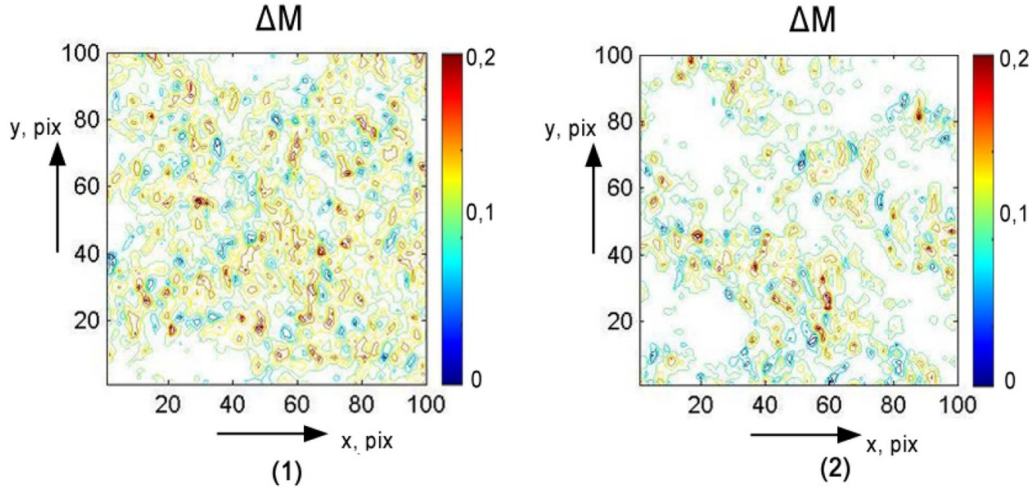
ΔM

Figure 3. Coordinate distributions of MMI **ΔM**, characterizing the circular birefringence **CB** of adenoma samples (fragment (1)) and carcinomas (fragment (2)) of the prostate.
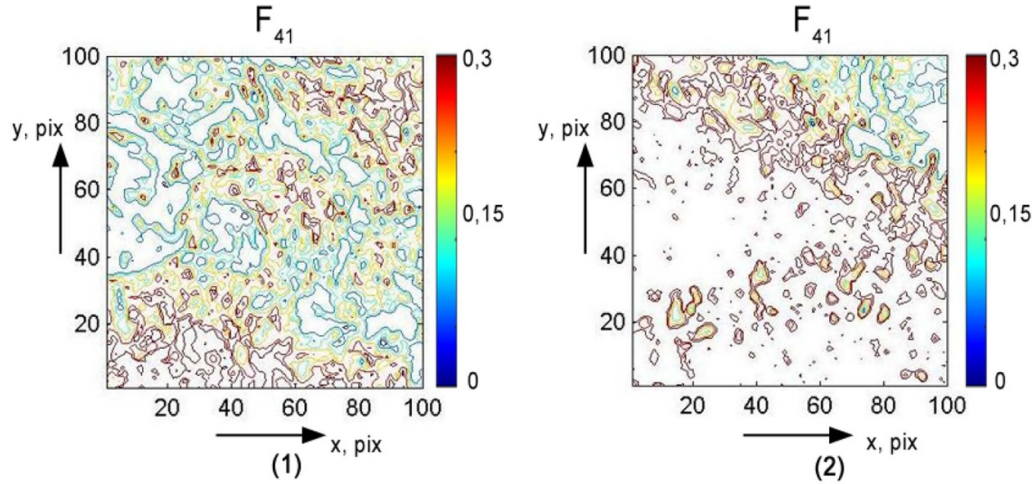
F₄₁

Figure 4. Coordinate distributions of MMI $\mathbf{F}_{41}$, characterizing the linear dichroism **LD** of adenoma samples (fragment (1)) and carcinomas (fragment (2)) of the prostate.

expect the following relationships between statistical moments [19, 24, 35, 38–43].

$$\begin{cases} \mathbf{Z}_{1;2}^{\mathbf{group1}} \left(\mathbf{F}_{44}\right) \prec \mathbf{Z}_{1;2}^{\mathbf{group2}} \left(\mathbf{F}_{44}\right); \\ \mathbf{Z}_{3;4}^{\mathbf{group1}} \left(\mathbf{F}_{44}\right) \prec \mathbf{Z}_{3;4}^{\mathbf{group2}} \left(\mathbf{F}_{44}\right); \end{cases} \quad (11)$$

$$\begin{cases} \mathbf{Z}_{1;2}^{\mathbf{group1}} \left(\mathbf{\Delta M}\right) \prec \mathbf{Z}_{1;2}^{\mathbf{group2}} \left(\mathbf{\Delta M}\right); \\ \mathbf{Z}_{3;4}^{\mathbf{group1}} \left(\mathbf{\Delta M}\right) \prec \mathbf{Z}_{3;4}^{\mathbf{group2}} \left(\mathbf{\Delta M}\right). \end{cases} \quad (12)$$

The most pronounced such scenario (relations (11), (12)) is realized in the scattering region of insignificant multiplicity, which corresponds to small values (0.3 *rad* ≺ φ ≺ 0.6 *rad* ⇒ φ* = 0.45 *rad*) of the phase cross sections of the MMI [$\mathbf{F}_{44}$; **ΔM**] (φ*, *m* × *n*).

For the linear (**LD** ~ sin **LB** (relation (3)) dichroism of the partially depolarizing layers of adenomas and carcinomas (figures 4 and 5) of the prostate decreases

$$\begin{cases} \mathbf{Z}_{1;2}^{\mathbf{group1}} \left(\mathbf{F}_{41}\right) \succ \mathbf{Z}_{1;2}^{\mathbf{group2}} \left(\mathbf{F}_{41}\right); \\ \mathbf{Z}_{3;4}^{\mathbf{group1}} \left(\mathbf{F}_{41}\right) \prec \mathbf{Z}_{3;4}^{\mathbf{group2}} \left(\mathbf{F}_{41}\right). \end{cases}$$

The circular (**CD** ↑, (equation (4)) dichroism of oncological changed prostate layers—increases

$$\begin{cases} \mathbf{Z}_{1;2}^{\mathbf{group1}} \left(\mathbf{F}_{14}\right) \succ \mathbf{Z}_{1;2}^{\mathbf{group2}} \left(\mathbf{F}_{14}\right); \\ \mathbf{Z}_{3;4}^{\mathbf{group1}} \left(\mathbf{F}_{14}\right) \prec \mathbf{Z}_{3;4}^{\mathbf{group2}} \left(\mathbf{F}_{14}\right). \end{cases}$$

The greatest difference between statistical moments $\mathbf{Z}_{\mathbf{i}=1;2;3;4} \left(\mathbf{F}_{41}; \mathbf{F}_{14}\right)$ is achieved in the range of somewhat larger values of the 'phase' cross sections (0.6 *rad* ≺ φ ≺ 0.9 *rad* ⇒ φ* = 0,75 *rad*).

Table 1 presents the statistical criteria for differentiating benign and malignant prostate tumors using 3D azimuthally invariant MM tomography [$\mathbf{F}_{44}$; **ΔM**; $\mathbf{F}_{41}$; $\mathbf{F}_{14}$] (φ, *m* × *n*).
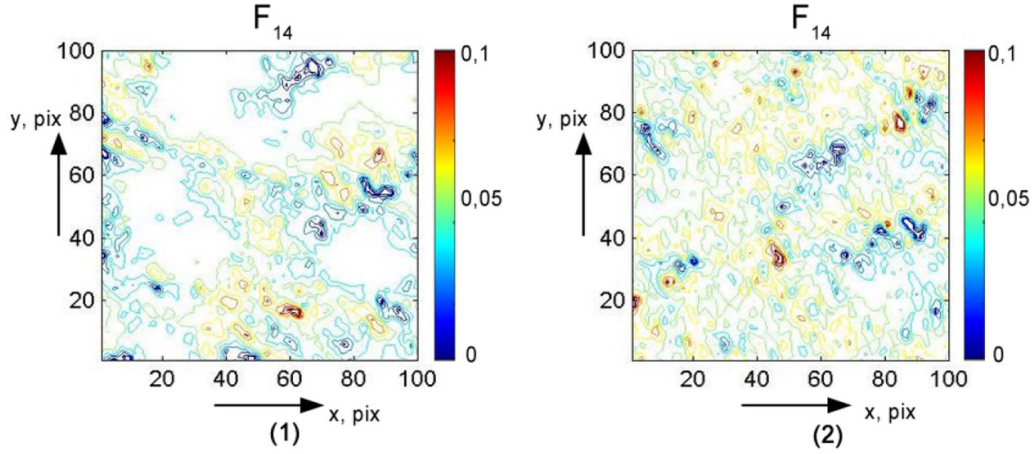
Figure 5. Coordinate distributions of MMI $\mathbf{F}_{14}$, characterizing the circular dichroism **CD** of adenoma samples (fragment (1)) and carcinomas (fragment (2)) of the prostate.

Table 1. The statistical moments of the 1st–4th order, which characterize the distributions of the MMI $[\mathbf{F}_{44};\mathbf{\Delta M};\mathbf{F}_{41};\mathbf{F}_{14}]\,(\phi^*, m \times n)$ set in diagnostically optimal phase sections ϕ^*.

Parameters	Adenoma		Carcinoma		Accuracy, $Ac,\%$	
MMI ($\phi^* = 0.45\,rad$)	$\mathbf{F}_{44}$	$\mathbf{\Delta M}$	$\mathbf{F}_{44}$	$\mathbf{\Delta M}$	$\mathbf{F}_{44}$	$\mathbf{\Delta M}$
$\mathbf{Z}_1$	0.29 ± 0.017	0.12 ± 0.007	0.44 ± 0.029	0.07 ± 0.004	85	82
$\mathbf{Z}_2$	0.21 ± 0.012	0.15 ± 0.008	0.14 ± 0.006	0.11 ± 0.005	81	79
$\mathbf{Z}_3$	0.46 ± 0.029	0.63 ± 0.041	0.69 ± 0.037	0.92 ± 0.055	91	89
$\mathbf{Z}_4$	0.57 ± 0.033	0.88 ± 0.053	1.03 ± 0.059	1.39 ± 0.084	92	87
MM ($\phi^* = 0.75\,rad$)	$\mathbf{F}_{41}$	$\mathbf{F}_{14}$	$\mathbf{F}_{41}$	$\mathbf{F}_{14}$	$\mathbf{F}_{41}$	$\mathbf{F}_{14}$
$\mathbf{Z}_1$	0.210 ± 013	0.0750 ± 0042	0.15 ± 0.091	0.093 ± 0.005	81	73
$\mathbf{Z}_2$	0.14 ± 0.008	0.09 ± 0.005	0.095 ± 0.006	0.12 ± 0.071	79	77
$\mathbf{Z}_3$	0.77 ± 0.043	0.98 ± 0.052	1.18 ± 0.063	0.61 ± 0.037	92	91
$\mathbf{Z}_4$	0.96 ± 0.054	1.31 ± 0.079	1.65 ± 0.093	0.99 ± 0.056	94	93

The most sensitive to the differences between the polycrystalline structure of the adenoma samples and the prostate carcinoma parameters have been identified—the statistical moments of the third and fourth orders, which characterize the asymmetry and kurtosis of the distributions $[\mathbf{F}_{44};\mathbf{\Delta M};\mathbf{F}_{41};\mathbf{F}_{14}]\,(\phi^*, m \times n)$.

For these parameters, according to the canons of evidence-based medicine [47], an excellent level of balanced accuracy of the 3D azimuthally invariant MM tomography method for partially depolarizing ($\Lambda \leqslant 50\%$) layers of biological tissues in differential diagnosis of benign and malignant prostate tumors was achieved $-\,\mathbf{Ac}\,(\mathbf{Z}_{3;4};(\mathbf{F}_{44;41;14},\mathbf{\Delta M})) \sim 91\% - 94\%$.

The result stimulated an additional study—the determination of the comparative efficacy of traditional [1–4, 12–15, 19–21, 24, 34, 35, 38–43] and the methods of polarimetric diagnostics proposed in this work, depending on the depolarizing ability of biological tissue samples.

5. Comparative characteristics of the diagnostic efficiency of the methods of polarization, 2D and 3D MM mapping

The comparative results of the diagnostic efficiency of differentiation of benign and malignant prostate tumors with different depolarizing ability by azimuthally invariant polarization [19, 38, 42–44, 46], 2D [20, 21, 24, 35, 38, 39, 41, 45] and 3D MM mapping. For this purpose, groups (16 samples each) of histological sections of adenoma biopsies and carcinomas with various geometric (l, μm), optical (τ) and depolarizing ($\Lambda, \%$) characteristics were studied.

Table 2 shows the maximum values of balanced accuracy, which are achieved by the methods considered.

From the comparative analysis of the accuracy of the polarimetric methods for diagnosing the changes in the phase and amplitude anisotropy of the depolarizing layers of benign and malignant prostate tumors:

(a) Polarization mapping of the azimuth (α) and ellipticity (β) polarization of the microscopic images of biological preparations ensures satisfactory accuracy of differentiation of adenoma and prostate carcinoma ($Ac\,(\tau = 0.25) = 76\% - 77\%$) to an insignificant level of depolarization ($\Lambda = 28\%$); for large values Λ this method is ineffective ($Ac \prec 70\%$).

(b) As the optical thickness ($0.25 \prec \tau \prec 0.62 \Leftrightarrow 28\% \prec \Lambda \prec 43\%$) of the samples increases, the accuracy of the method of azimuthally-invariant 2D MM mapping

Table 2. Comparative diagnostic effectiveness of azimuthal invariant polarimetry methods.

τ		0.25			0.45			0.62	
$l, \mu m$		20			40			50	
$\Lambda, \%$		28			35			43	
$Ac, \%$	$\{\alpha,\beta\}$	2D	3D	$\{\alpha,\beta\}$	2D	3D	$\{\alpha,\beta\}$	2D	3D
$Ac(\mathbf{Z}_1)$	73	78	91	69	71	87	63	65	85
$Ac(\mathbf{Z}_2)$	76	79	93	70	74	89	65	68	87
$Ac(\mathbf{Z}_3)$	76	84	95	72	77	95	68	71	93
$Ac(\mathbf{Z}_4)$	77	83	96	73	79	95	70	75	94
τ		0.91			1.37			1.93	
$l, \mu m$		60			80			100	
$\Lambda, \%$		52			68			89	
$Ac, \%$	$\{\alpha,\beta\}$	2D	3D	$\{\alpha,\beta\}$	2D	3D	$\{\alpha,\beta\}$	2D	3D
$Ac(\mathbf{Z}_1)$	59	63	83	53	57	64	54	53	52
$Ac(\mathbf{Z}_2)$	58	65	85	55	56	66	52	56	54
$Ac(\mathbf{Z}_3)$	61	68	91	57	59	78	53	57	65
$Ac(\mathbf{Z}_4)$	63	69	94	56	63	79	55	60	68

decreases from good ($Ac(\tau = 0.25; \Lambda = 28\%) = 83\% - 84\%$) to satisfactory ($Ac(\tau = 0.62; \Lambda = 43\%) = 75\%$)).

(c) Azimuthal invariant 3D MM tomography proved to be the most diagnostically effective ($70\% \prec Ac \prec 96\%$) in a wide range of optical thickness ($0.25 \prec \tau \prec 1.37 \Leftrightarrow 28\% \prec \Lambda \prec 68\%$) histological sections of biopsy of benign and malignant tumors of the prostate.

6. Conclusion

A method of azimuthally-invariant 3D MM tomography of phase and amplitude anisotropy of partially depolarizing layers of the prostate benign and malignant tumors is proposed and justified.

Layered 'phase' dependences of the magnitude of the statistical moments of the 1st–4th order, which characterize the MMI $[\mathbf{F}_{44}; \mathbf{\Delta M}; \mathbf{F}_{41}; \mathbf{F}_{14}](\phi_k, m \times n)$ of the polycrystalline component of the histological sections of prostate tumors, were investigated.

Optimal conditions for differentiation of polycrystalline structures of benign and malignant tumors—the range of phase sections $\begin{cases} \phi^*(\mathbf{F}_{44}; \mathbf{\Delta M}) = 0.45\, rad; \\ \phi^*(\mathbf{F}_{41}; \mathbf{F}_{14}) = 0.75\, rad \end{cases}$ and the most sensitive parameters $\Delta Z^*_{\mathbf{i}=3;4}(\mathbf{F}_{44}; \mathbf{\Delta M}; \mathbf{F}_{41}; \mathbf{F}_{14}) \equiv \Delta \mathbf{Z}_{\mathbf{i}=3;4}(\phi^*) \rightarrow$ max (statistical moments of the 3rd and 4th orders) are revealed.

Statistical analysis of the distributions of the parameters of phase ($\mathbf{LB}, \mathbf{CB}$) and amplitude ($\mathbf{LD}, \mathbf{CD}$) anisotropy $[\mathbf{F}_{44}; \mathbf{\Delta M}; \mathbf{F}_{41}; \mathbf{F}_{14}](\phi^*, m \times n)$ provided an excellent good balanced accuracy ($\mathbf{Ac}(\mathbf{Z}_{3;4}[\mathbf{F}_{44}; \mathbf{\Delta M}; \mathbf{F}_{41}; \mathbf{F}_{14}]) \sim 91\% - 94\%$) of differential diagnosis of prostate tumors.

Comparative studies of the diagnostic efficiency of azimuthally-invariant methods of polarization, 2D and 3D MM mapping of prostate tumor samples with different optical thickness (τ) and depolarizing ability (Λ) were carried out. On this basis, the levels of balanced accuracy (**Ac**) and limits ($0.25 \prec \tau \prec 1.37 \Leftrightarrow 28\% \prec \Lambda \prec 68\%$) of using the methods are determined.

Disclosures

The presenting authors do not have any financial conflicts of interest regarding the content of this manuscript.

References

[1] Novikova T, Meglinski I, Romella-Roman J and Tuchin V V 2016 Polarized light for biomedical applications *J. Biomed. Opt.* **21** 071001

[2] Bachinskyi V, Boychuk T and Ushenko A 2018 *Laser Polyrimetry of Biological Tissues and Fluids* (Riga: Lap Lambert Academic publishing)

[3] Bachinskyi V T, Wanchulyak O Y, Ushenko A G, Ushenko Y A, Dubolazov A V and Meglinski I 2020 *Polarization Correlometry of Scattering Biological Tissues and Fluids* (Singapore: Springer)

[4] Ghosh N and Vitkin I A 2011 Tissue polarimetry: concepts, challenges, applications and outlook *J. Biomed. Opt.* **16** 110801

[5] Layden D, Ghosh N and Vitkin A 2013 Quantitative polarimetry for tissue characterization and diagnosis *Advanced Biophotonics: Tissue Optical Sectioning*, ed R K Wang and V V Tuchin (Boca Raton, FL: CRC Press) pp 73–108

[6] Vitkin A, Ghosh N and De Martino A 2015 Tissue polarimetry *Photonics: Scientific Foundations, Technology and Applications* Vol. IV, ed D L Andrews (Hoboken, NJ: Wiley) pp 239–321

[7] Mishchenko M I, Travis L D and Lacis A A 2002 *Scattering, Absorption, and Emission of Light by Small Particles* (Cambridge: Cambridge University Press)

[8] Swami M K, Patel H S and Gupta P K 2013 Conversion of 3×3 Mueller matrix to 4×4 Mueller matrix for non-depolarizing samples *Opt. Commun.* **286** 18–22

[9] Izotova V F, Maksimova I L, Nefedov I S and Romanov S V 1997 Investigation of Mueller matrices of anisotropic nonhomogeneous layers in application to optical model of cornea *Appl. Opt.* **36** 164–9

[10] Doronin A, Vera N, Staforelli J P, Coelho P and Meglinski I 2019 Propagation of cylindrical vector laser beams in turbid tissue-like scattering medium *Photonics* **6** 56

[11] Doronin A, Radosevich A J, Backman V and Meglinski I 2014 Two electric field Monte Carlo models of coherent backscattering of polarized light *J. Opt. Soc. Am.* A **31** 2394–400

[12] Doronin A, Macdonald C and Meglinski I 2014 Propagation of coherent polarized light in highly scattering turbid media *J. Biomed. Opt.* **19** 025005

[13] Meglinski I, Kirillin M, Kuzmin V L and Myllyla R 2008
Simulation of polarization-sensitive optical coherence
tomography images by a Monte Carlo method *Opt. Lett.*
33 1581–3

[14] Antonelli M R, Pierangelo A, Novikova T, Validire P,
Benali A, Gayet B and De Martino A 2011 Impact of model
parameters on Monte Carlo simulations of backscattering
Mueller matrix images of colon tissue *Biomed. Opt. Express*
2 1836–51

[15] Antonelli M R, Pierangelo A, Novikova T, Validire P,
Benali A, Gayet B and De Martino A 2010 Mueller matrix
imaging of human colon tissue for cancer diagnostics: how
Monte Carlo modeling can help in the interpretation of
experimental data *Opt. Express* **18** 10200–8

[16] Vitkin I A and Studinski R C N 2001 Polarization preservation
in diffusive scattering from in vivo turbid biological media:
effects of tissue optical absorption in the exact
backscattering direction *Opt. Commun.* **190** 37–43

[17] Das N K, Dey R, Chakraborty S, Panigrahi P K, Meglinski I
and Ghosh N 2018 Quantitative assessment of submicron
scale anisotropy in tissue multifractality by scattering
Mueller matrix in the framework of Born approximation
Opt. Commun. **413** 172–8

[18] Das N K, Dey R, Chakraborty S, Panigrahi P K, Meglinski I
and Ghosh N 2018 Submicron scale tissue multifractal
anisotropy in polarized laser light scattering *Laser Phys.
Lett.* **15** 035601

[19] Ushenko V *et al* 2018 3D Mueller-matrix diffusive
tomography of polycrystalline blood films for cancer
diagnosis *Photonics* **5** 54

[20] Deng Y, Zeng S, Lu Q, Zhu D and Luo Q 2007
Characterization of backscattering Mueller matrix patterns
of highly scattering media with triple scattering assumption
Opt. Express **15** 9672–80

[21] Ushenko A G and Pishak V P 2004 Laser polarimetry of
biological tissue: principles and applications *Handbook of
Coherent-Domain Optical Methods: Biomedical
Diagnostics, Environmental and Material Science* Vol. I,
ed V V Tuchin (Boston: Kluwer Academic Publishers) pp
93–138

[22] Angelsky O V *et al* 2010 Statistical, correlation and
topological approaches in diagnostics of the structure and
physiological state of birefringent biological tissues
Handbook of Photonics for Biomedical Science, ed
V V Tuchin (Boca Raton, FL: CRC Press) pp 283–322

[23] Ushenko Y A *et al* 2013 Diagnostics of structure and
physiological state of birefringent biological tissues:
statistical, correlation and topological approaches
Handbook of Coherent-Domain Optical Methods (New
York: Springer) p 107

[24] Lu S Y and Chipman R A 1996 Interpretation of Mueller
matrices based on polar decomposition *J. Opt. Soc. Am.* A
13 1106–13

[25] Agarwal N, Yoon J, Garcia-Caurel E, Novikova T, Vanel J-C,
Pierangelo A, Bykov A, Popov A, Meglinski I and
Ossikovski R 2015 Spatial evolution of depolarization in
homogeneous turbid media within the differential Mueller
matrix formalism *Opt. Lett.* **40** 5634–7

[26] Borovkova M, Peyvasteh M, Dubolazov O, Ushenko Y,
Ushenko V, Bykov A, Deby S, Rehbinder J, Novikova T and
Meglinski I 2018 Complementary analysis of Muller-matrix
images of optically anisotropic highly scattering biological
tissues *J. Eur. Opt. Soc: Rapid Publ.* **14** 20

[27] Borovkova M *et al* 2019 Mueller-matrix-based polarization
imaging and quantitative assessment of optically
anisotropic polycrystalline networks *PloS One*
14 e0214494

[28] Manhas S, Vizet J, Deby S, Vanel J-C, Boito P, Verdier M,
De Martino A and Pagnoux D 2015 Demonstration of full

4 × 4 Mueller polarimetry through an optical fiber for
endoscopic applications *Opt. Express* **23** 3047–54

[29] Pierangelo A, Manhas S, Benali A, Fallet C, Totobenazara J-L,
Antonelli M-R, Novikova T, Gayet B, De Martino A and
Validire P 2013 Multispectral Mueller polarimetric imaging
detecting residual cancer and cancer regression after
neoadjuvant treatment for colorectal carcinomas *J. Biomed.
Opt.* **18** 046014

[30] Wang L V and Wu H I 2007 *Biomedical Optics: Principles
and Imaging* (Hoboken, NJ: Wiley)

[31] Boas D, Pitris C and Ramanujam N 2011 *Handbook of
Biomedical Optics* (Boca Raton, FL: CRC Press)

[32] Vo-Dinh T 2014 *Biomedical Photonics Handbook* 2nd edn
(Boca Raton, FL: CRC Press)

[33] Tuchin V V 2015 *Tissue Optics: Light Scattering Methods and
Instruments for Medical Diagnostics* 3rd edn (Bellingham,
WA: SPIE Press) p PM 254

[34] Jacques S L 2011 Polarized light imaging of biological tissues
Handbook of Biomedical Optics, ed D Boas, C Pitris and N
Ramanujam (Boca Raton, FL: CRC Press)
pp 649–69

[35] Ghosh N, Wood M and Vitkin A 2010 Polarized light
assessment of complex turbid media such as biological
tissues using Mueller matrix decomposition *Handbook of
Photonics for Biomedical Science*, ed V V Tuchin (London:
Taylor and Francis Publishing) chapter 9,
pp 253–82

[36] Kasaragod D K, Lu Z, Jacobs J and Matcher S J 2012
Experimental validation of an extended Jones matrix
calculus model to study the 3D structural orientation of the
collagen fibers in articular cartilage using
polarization-sensitive optical coherence tomography
Biomed. Opt. Express **3** 378–87

[37] Yasuno Y *et al* 2015 Jones Matrix based polarization sensitive
optical coherence tomography *Optical Coherence
Tomography: Technology and Applications* 2nd edn, ed
W Drexler and J G Fujimoto (Cham: Springer)
pp 1137–62

[38] Ushenko V A and Gavrylyak M S 2013 Azimuthally invariant
Mueller-matrix mapping of biological tissue in differential
diagnosis of mechanisms protein molecules networks
anisotropy *Proc. SPIE 8812 Biosensing and Nanomedicine*
vol VI pp 88120Y

[39] Ushenko V A and Dubolazov A V 2013 Correlation and self
similarity structure of polycrystalline network biological
layers Mueller matrices images *Proc. SPIE*
8856 88562D 6

[40] Ushenko V A, Pavlyukovich N D and Trifonyuk L 2013
Spatial-frequency azimuthally stable cartography of
biological polycrystalline networks *Int. J. Opt.* **2013** 7

[41] Ushenko V A *et al* 2013 Mueller-matrices polarization
selection of two-dimensional linear and circular
birefringence images *Eleventh Int. Conf. on Correlation
Optics Proc. SPIE* vol 9066 p 90661X

[42] Ushenko V A and Gorsky M P 2013 Complex degree of
mutual anisotropy of linear birefringence and optical
activity of biological tissues in diagnostics of prostate
cancer *Opt. Spectrosc.* **115** 290–7

[43] Ushenko Y A, Ushenko V A, Dubolazov A V,
Balanetskaya V O and Zabolotna N I 2012 Mueller-matrix
diagnostics of optical properties of polycrystalline networks
of human blood plasma *Opt. Spectrosc.* **112** 884–92

[44] Ushenko Y A, Dubolazov A V, Balanetskaya V O,
Karachevtsev A O and Ushenko V A 2012 Wavelet-analysis
of polarization maps of human blood plasma *Opt.
Spectrosc.* **113** 332–43

[45] Ushenko V O 2013 Spatial-frequency polarization phasometry
of biological polycrystalline networks *Opt. Mem. Neural
Netw.* **22** 56–64

[46] Ungurian V P, Ivashchuk O I and Ushenko V O 2011 Statistical analysis of polarizing maps of blood plasma laser images for the diagnostics of malignant formations *Proc. SPIE* **8338** 83381L

[47] Ushenko V A, Dubolazov O V and Karachevtsev A O 2014 Two wavelength Mueller matrix reconstruction of blood plasma films polycrystalline structure in diagnostics of breast cancer *Appl. Opt.* **53** B128–39